Towards simulating star formation in the interstellar medium

Adrianne D. Slyz,[1]* Julien E. G. Devriendt,[1,2] Greg Bryan[1] and Joseph Silk[1]

[1]*Astrophysics, Keble Road, Oxford OX1 3RH*
[2]*CRAL-Observatoire, 9 Avenue Charles-André, 69561 Saint-Genis-Laval, France*

ABSTRACT

As a first step to a more complete understanding of the local physical processes which determine star formation rates (SFRs) in the interstellar medium (ISM), we have performed controlled numerical experiments consisting of hydrodynamical simulations of a kiloparsec-scale, periodic, highly supersonic and 'turbulent' three-dimensional flow. Using simple but physically motivated recipes for identifying star-forming regions, we convert gas into stars which we follow self-consistently as they impact their surroundings through supernovae and stellar winds. We investigate how various processes (turbulence, radiative cooling, self-gravity, and supernovae feedback) structure the ISM, determine its energetics, and consequently affect its SFR. We find that the one-point statistical measurement captured by the probability density function (PDF) is sensitive to the simulated physics. The PDF is consistent with a log-normal distribution for the runs which remove gas for star formation and have radiative cooling, but implement neither supernovae feedback nor self-gravity. In this case, the dispersion, σ_s, of the log-normal decays with time and scales with $\sqrt{\ln[1 + (M_{rms}/2)^2]}$ where M_{rms} is the root-mean-squared Mach number of the simulation volume, $s = \ln \rho$, and ρ is the gas density. With the addition of self-gravity, the log-normal consistently underpredicts the high-density end of the PDF which approaches a power law. With supernovae feedback, regardless of whether we consider self-gravity or not, the PDF becomes markedly bimodal with most of the simulation volume occupied by low-density gas. Aside from its effect on the density structure of the medium, including self-gravity and/or supernovae feedback changes the dynamics of the medium by halting the decay of the kinetic energy. Since we find that the SFR depends most strongly on the underlying velocity field, the SFR declines in the runs lacking a means to sustain the kinetic energy, and the subsequent high density contrasts. This strong dependence on the gas velocity dispersion is in agreement with Silk's formula for the SFR which also takes the hot gas porosity, and the average gas density as important parameters. Measuring the porosity of the hot gas for the runs with supernovae feedback, we compare Silk's model for the SFR to our measured SFR and find agreement to better than a factor two.

Key words: hydrodynamics – methods: numerical – stars: formation – ISM: theory – galaxies: general.

1 INTRODUCTION

The correlation in galaxies between the star formation rate (SFR) and the average gas surface density over several orders of magnitude (Kennicutt 1998) suggests a simple, deterministic prescription (Schmidt 1959) for star formation. Yet the finding that, at least in the Milky Way, all star formation occurs in dense, cold clouds of molecular hydrogen and dust raises the question of how information about the average gas density of a galaxy reaches the small scale on which star formation occurs. Furthermore, observations of our

own interstellar medium (ISM) as well as that of other galaxies reveal that far from being well described by a global quantity like the average gas density, the ISM has a spectacularly complex structure on many scales. Diffuse ionized gas in edge-on spirals is concentrated in webs of filaments and shells (Rand, Kulkarni & Hester 1990; Dettmar 1992; Ferguson, Wyse & Gallagher 1996). Atomic gas detected by 21-cm emission in our Galaxy (Heiles 1979, 1984) as well as in several other spirals (Rand & van der Hulst 1993; Irwin 1994; King & Irwin 1997; Lee & Irwin 1997) resides in 'supershells' and 'worms'. In maps of the nearby spirals M31 and M33 (Brinks & Bajaja 1986; Deul & den Hartog 1990), it is also found to be depleted in numerous 100 pc–1 kpc 'holes'. Attempts to quantify this elaborate ISM structure are confronted with questions of identification.

*E-mail: slyz@astro.ox.ac.uk

Structures are interconnected, with, for example, denser regions of gas embedded within filaments. Hence, for example, potential sites of star formation cannot be picked out, without introducing a density threshold and thereby a bias to separate them from the underlying density field. An alternative way to analyse the ISM is with Fourier transform power spectra. Applied to H I emission maps of the Large and Small Magellanic Clouds, power laws over approximately two orders of magnitude are found (Stanimirovic et al. 1999; Elmegreen, Kim & Stavely-Smith 2001), providing another insight into the structure of the ISM, namely that as other observations have already suggested, it is likely to be turbulent.

Clues about the energy sources for the stirring of the ISM come from measurements of the sizes and velocities of shells. In some cases stellar winds and supernovae are found to be adequate for creating the supershells, and H I holes. In other cases larger quantities of energy are demanded and then collisions of external clouds with the galaxies are invoked (Tenorio-Tagle 1981). As for the diffuse ionized medium, although the energy available from O stars would be sufficient to account for its photoionization, a well-known problem is that photons from the O stars cannot travel far from their origin without being absorbed by the molecular clouds and H I haloes surrounding them. In that case the photons either reach larger distances by travelling through photoionized conduits carved out by earlier supernovae or as suggested by an alternative model they are additionally generated in turbulent mixing layers at the interfaces between hot and cold gas. These are ubiquitous in the ISM, and have been invoked as an efficient means to convert the thermal energy generated by shear flows to ionizing radiation (Begelman & Fabin 1990; Slavin, Shull & Begelman 1993). Ultimately the energy source in the latter model is again the supernovae which create the hot gas. Recent X-ray images from *Chandra* map out this hot, tenuous gas, predicted by Spitzer (1956), above and below the galactic plane of disc galaxies (Wang et al. 2001). Even without a heat source, due to its long cooling time, once it is generated by supernovae, such gas can persist for millions of years. Cox & Smith (1974) reasoned that given that OB stars occur in associations, it is likely that a supernova will go off inside the hot cavity generated by a previous supernova, thereby rejuvenating it and creating an even larger cavity. In this way, successive supernovae can overlap, creating a network of tunnels. Expanding at high speed within these tunnels, the hot gas can move above the galactic plane where it is either halted by insufficient speed to escape the galactic potential, or by an encounter with a large mass of cold, high-density gas, or by efficient mixing with cooler gas which increases its density thereby accelerating its radiative energy losses.

In light of this complex environment in which star formation occurs, it is even more surprising that the Schmidt law is so successful. It is in the context of this complexity that we undertake a study of the star formation rate in a multiphase ISM. We restrict ourselves to a local study of the ISM, namely that of a ~ 1 kpc^3 region. The earliest local study which included supernovae feedback was done by Rosen & Bregman (1995) in two dimensions. They considered a segment of a galactic disc, taking into account a fixed external gravitational potential, but neglecting rotational effects, self-gravity and magnetic fields. In a three-dimensional model which included the effects of an external gravitational potential, rotation, and magnetic fields, Korpi et al. (1999a,b) studied a supernova-driven galactic dynamo. Meanwhile, to investigate the disc–halo interaction, Avillez (2000) followed the evolution of a segment of a galactic disc with an adaptive mesh refinement code. Unlike these studies, ours follows self-consistently and in three dimensions both the gas and the stars, treating the latter as a system of collisionless particles subject to

gravity. Rosen & Bregman (1995) followed the stellar component but treated the stars with the same fluid equations used for the gas, thereby making their flow more viscous than that expected for a collisionless system of particles. Without star particles tagged with their ages, Rosen & Bregman (1995) decided upon a supernovae rate for their simulation, then proceeded to set off supernovae with a probability of occurrence correlated to the stellar density. Avillez (2000) approached the issue by constructing an algorithm to distinguish between isolated and clustered supernovae. For isolated supernovae events, Avillez (2000) randomly determined the positions of supernovae in the disc plane with rates based on observed ones. To mimic clustered supernovae, a percentage of the supernovae sites were chosen to coincide with locations where there was a previous supernova. In the Korpi et al. (1999a,b) implementation there was a density criterion to determine the locations of isolated supernovae. In both Avillez (2000) and Korpi et al. (1999a,b), supernovae occurring above the disc plane were placed in random locations with an exponential distribution characterized by a scale-height also adopted from observations. Given that we are interested in the impact of supernovae feedback on star formation, we cannot rely on these methods of modelling the locations of supernovae. Instead we require that the locations, ages and masses of the star particles self-consistently determine the supernovae events. A simple calculation shows that a star with a velocity of 10 km s^{-1} will travel ~ 100 pc (e.g. the average size of a molecular cloud) in 10 Myr. The latter corresponds to a typical time delay between the birth and death of a star with $M \sim 80\,M_\odot$. In a follow-up paper we explore how our results change when we neglect this time delay and instead allow the stars to explode as supernovae immediately after their birth (Slyz, Devriendt, Bryan & Silk, in preparation). Obviously a local model such as ours is of limited relevance for quantitative comparisons to the ISM in galaxies. As later detailed in Section 6, the limitations of our idealized boundary conditions and the absence in our models of an external gravitational potential as well as of a shear flow arising from rotation means that there are many fundamental questions that we cannot address. Nevertheless we believe that for the purposes of studying the non-linear interplay between star formation and stellar feedback, our simple model yields important insights.

The question we address is what physical processes regulate the rate at which gas turns into stars in a multiphase ISM. In Section 2 we describe the numerical method we use as well as the ingredients of our simulation. To model the large dynamic range in densities and temperatures of a gaseous medium compressed by self-gravity and by shocks maintained by supernovae and stellar winds, a robust high-resolution hydrodynamical scheme proves essential. To get a qualitative idea about the phenomena involved, Section 3 presents the general morphological, thermodynamical, and dynamical features of our simulations. A more quantitative analysis of the gas structure and dynamics is presented in Section 4 where we explore changes in the gas probability density function and energy spectra with the addition of more and more physics thought to be relevant for star formation. Section 5 compares the star formation rates we measure in our simulations to simple analytic prescriptions and Section 6 discusses the limitations of our simulations. Finally our main conclusions are summarized in Section 7.

2 METHOD AND INGREDIENTS OF THE SIMULATIONS

Traditionally the problem with numerical simulations trying to model star formation and feedback processes is that the radiative

losses of the hot component generated by supernovae are enormous, even though in the absence of any interaction of the hot gas with the cold gas the cooling time of the hot gas is on the order of 100 Myr. In many cases the culprit is numerical diffusion which mixes cold gas into the hot gas more than it physically should. As a result, since the density of the cold gas is high, mixing even a small fraction of it with the low-density hot gas increases the density of the hot component sufficiently for it to cool more efficiently than it should. For this reason, high-resolution grid codes are better suited for studies of the multiphase interstellar medium than more diffusive particle-based methods which require carefully constructed algorithms to circumvent artificial cooling (e.g. Marri & White 2003).

With this in mind, we model the evolution of gas and stars in a three-dimensional periodic box which is 1.28 kpc on a side with a grid-based scheme for the gas and a particle-mesh method for the stars. More specifically we have incorporated the BGK hydrocode (Prendergast & Xu 1993; Slyz & Prendergast 1999) into Bryan's ENZO code (Bryan & Norman 1997, 1999) which uses a Lagrangean particle-mesh (PM) algorithm to follow the collisionless stars moving in the gravitational potential the gas and the stars themselves generate. Based on gas-kinetic theory, BGK computes time-dependent hydrodynamical fluxes from velocity moments of a distribution function which is a local solution to a model of the collisional Boltzmann equation, namely the BGK equation (Bhatnagar, Gross & Krook 1954). The hydrodynamics code has been extensively tested on discontinuous non-equilibrium flows (see Xu 1998, for a review) and performs well both at flow discontinuities and strongly rarefied regions, a criterion which is mandatory for ISM simulations.

Initially the gas has constant density ($\rho_{\rm gas} = 1$ atom cm^{-3}) and temperature ($T_{\rm gas} = 10^5$ K) and, similar to the initialization in MacLow et al. (1998), its velocity field is drawn from a Gaussian random field characterized by a power spectrum scaling like k^{-4}. We truncate this velocity power spectrum so that the field only has power on large scales, i.e. in modes up to $k = 4$. The initial $v_{\rm rms}$ is ~50 km s^{-1}. Contrary to MacLow et al. (1998), we do not add velocity perturbations at each time-step to drive the 'turbulence'. We only impose the velocity perturbations once at the beginning of the simulation. We assume radiative cooling of an optically thin gas which is in collisional ionization equilibrium. More specifically, our cooling function, displayed in Fig. 1, is an extension of the cooling curve of Sarazin & White (1987) down to temperatures of $T_{\rm min} = 310$ K to account for H$_2$ cooling using the rates given in Rosen & Bregman (1995). The extension to lower temperatures assumes a solar metallicity, a completely ionized gas at 8000 K and an ionization fraction that gradually drops to 10^{-3} below 8000 K. Fitting a piecewise power law to our cooling curve gives:

$\Lambda(T)$

$$= \begin{cases} 0 & \text{if } T < 310 \text{ K,} \\ (2.2380 \times 10^{-32})T^2 & \text{if } 310 \leqslant T < 2000 \text{ K} \\ (1.0012 \times 10^{-30})T^{1.5} & \text{if } 2000 \leqslant T < 8000 \text{ K} \\ (4.6240 \times 10^{-36})T^{2.867} & \text{if } 8000 \leqslant T < 39\,811 \text{ K} \\ (3.1620 \times 10^{-30})T^{1.6} & \text{if } 39\,811 \leqslant T < 10^5 \text{ K} \\ (3.1620 \times 10^{-21})T^{-0.2} & \text{if } 10^5 \leqslant T < 2.884 \times 10^5 \text{ K} \\ (6.3100 \times 10^{-6})T^{-3} & \text{if } 2.884 \times 10^5 \leqslant T < 4.732 \times 10^5 \text{ K} \\ (1.047 \times 10^{-21})T^{-0.22} & \text{if } 4.732 \times 10^5 \leqslant T < 2.113 \times 10^6 \text{ K} \\ (3.981 \times 10^{-4})T^{-3} & \text{if } 2.113 \times 10^6 \leqslant T < 3.981 \times 10^6 \text{ K} \\ (4.169 \times 10^{-26})T^{0.33} & \text{if } 3.981 \times 10^6 \leqslant T < 1.995 \times 10^7 \text{ K} \\ (2.399 \times 10^{-27})T^{0.5} & \text{if } T \geqslant 1.995 \times 10^7 \text{ K.} \end{cases}$$
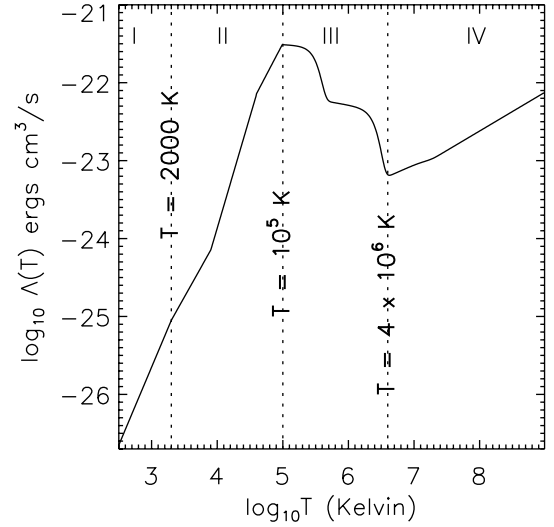
Figure 1. Cooling curve with vertical dotted lines overplotted to delineate several different temperature regimes which we consider in Section 3.

The lower temperature cut-off of the cooling function at 310 K is unphysical, although Rosen, Bregman & Norman (1993) argue that truncating it there is a way to model the contribution to the ISM pressure from sources such as magnetic fields and cosmic rays, which do not decrease as the gas radiatively cools.

2.1 Implementation of star formation and feedback

Following Cen & Ostriker (1992), we assume that star formation is inevitable if a region is contracting ($\nabla \cdot v < 0$), cooling rapidly ($t_{\rm cool} < t_{\rm dyn}$ and $T_{\rm gas} \leqslant T_{\rm min}$), and is overdense ($\rho > \rho_{\rm crit}$). Since we check the grid on a cell-by-cell basis to see if these conditions are met, each time-scale is computed for each grid cell. Here $t_{\rm dyn}$ is the dynamical collapse time-scale, i.e. $t_{\rm dyn} = \sqrt{3.0\pi/(32 G \rho_{\rm tot})}$ where $\rho_{\rm tot}$ is the sum of the gas density, ρ, and the stellar density. $t_{\rm cool}$ is the cooling time-scale, i.e. $t_{\rm cool} = kT / n\Lambda$, where n is the gas particle number density. $T_{\rm min}$ is the minimum of our cooling curve, 310 K, and $\rho_{\rm crit}$ for the different simulations is specified in Table 1. If all our star-forming criteria are met within a grid cell then we convert the following amount of gas

$$\Delta m_{\rm gas} = \epsilon \frac{\Delta t}{t_{\rm dyn}} \rho_{\rm gas} \Delta x^3,$$

into a 'star particle', where ϵ is a star formation efficiency parameter which we take to be 0.1 unless otherwise stated, and Δt is the updating time-step. We only allow at maximum 90 per cent of the gas in a cell to be converted to stars in one time-step. In practice, however, once supernovae inject hot gas into the medium, the updating time-step is short as it is set by the hot, low-density gas. As a result $\Delta t < t_{\rm dyn}$, and this 90 per cent threshold is never reached. We give the new star particle the same velocity as the gas out of which it formed and we follow the stars dynamically. The star particle is labelled with its mass, $m_\star$, its formation time, $t_{\rm SF}$, and the dynamical time, $t_{\rm dyn}$, of the gas out of which it formed.

For the purposes of the feedback, however, rather than assume that the 'star particle' formed instantaneously at $t_{\rm SF}$, we spread the star formation over several dynamical times by computing the amount of gas mass that would form stars after time $t_{\rm SF}$ to be:

$$\Delta m_{\rm stars}(t) = m_\star \frac{(t - t_{\rm SF})}{\tau^2} \exp\left[\frac{-(t - t_{\rm SF})}{\tau}\right] \tag{1}$$

Table 1. Summary of the performed runs. All of the runs have radiative cooling. The first three columns indicate whether self-gravity, star formation and/or feedback are activated. ρ_{crit} is the density threshold for star formation, ϵ is the star formation efficiency and the final column indicates the grid resolution. Each simulation cube is 1.28 kpc per side.

	Self-gravity	Stars	Feedback	ρ_{crit} (at cm^{-3})	ϵ	Grid resolution (pc)
A	–	–	–	–	–	5
B1	–	yes	–	10.	0.1	10
B2	yes	yes	–	10.	0.1	10
B3	–	yes	yes	10.	0.1	10
B4	yes	yes	yes	10.	0.1	10
B5	yes	yes	yes	1.	0.1	10
B6	yes	yes	yes	10.	0.01	10
C1	–	yes	–	10.	0.1	20
C2	yes	yes	–	10.	0.1	20
C3	–	yes	yes	10.	0.1	20
C4	yes	yes	yes	10.	0.1	20
C5	yes	yes	yes	1.	0.1	20
C6	yes	yes	yes	1.	0.01	20

where $\tau = \max(t_{dyn}, 10\,\mathrm{Myr})$. With this time-dependent star formation rate, stars form at an exponentially decreasing rate after a dynamical time. If the dynamical time-scale of the gas in a star-forming cell is shorter than the typical lifespan of a massive star, i.e. 10 Myr, then 10 Myr is used in place of t_{dyn} in equation (1) for the value of τ. Then, as a crude model of a stellar wind, we return 25 per cent of Δm_{stars} to the gas, and since this returned mass has the velocity of the 'star particle' we alter the momentum of the gas appropriately. Finally assuming only the occurrence of Type II supernovae, we add 10^{-5} of the rest-mass energy of Δm_{stars} to the thermal energy of the gas (Ostriker & Cowie 1981). The supernovae input is added locally into one cell. We explore the limitations of our supernovae implementation in future work. As we do not have the resolution to follow every individual star and therefore to sample a realistic initial mass function (IMF) for them, each star particle is more like a small star cluster with a typical mass in the range $\sim$120–220 $M_\odot$.

Table 1 presents the simulations we ran, listing the values of the parameters for star formation and feedback. Although we performed several simulations with a density threshold for star formation, ρ_{crit}, set to 1 atom cm^{-3} (runs B5, C5 and C6), for the remainder of the paper we focus only on the runs with $\rho_{crit} = 10$ atom cm^{-3}. This is because we found that dropping the density threshold by one order of magnitude to 1 atom cm^{-3} did not change the SFR by a factor 10, but merely by about 10 per cent at the peak of star formation. As Table 1 indicates, we also experimented with the value of ϵ and found that taking a value of $\epsilon = 0.01$ (10 times smaller than our fiducial value) left the conclusions presented in this paper unchanged, i.e. the medium became porous and the SFR peaked at roughly the same value although with a slight time delay compared to the run with $\epsilon = 0.1$.

3 GENERAL FEATURES OF THE MULTIPHASE MEDIUM

We begin by showing the time evolution of one of our simulations, namely B4, which includes all the physical processes we considered, namely 'turbulent' initial conditions (as defined in Section 2), radiative cooling, self-gravity, star formation and feedback. In Fig. 2 we show the gas density, temperature and pressure in a 12.8 pc $\times$ 1.28 kpc $\times$ 1.28 kpc slice of this run. Due to the compression caused by turbulence and self-gravity, the gas in certain regions sat-

isfies our criteria for star formation. Following their formation, this first generation of stars soon explodes as supernovae, releasing hot gas into the interstellar medium. The morphologies of the hot bubbles are extremely non-spherical due to the fact that the supernovae are releasing their thermal energy into a spatially inhomogeneous and non-stationary medium. Because this hot, low-density gas has a long cooling time and because the star formation rate is sufficiently high, subsequent generations of supernovae bubbles overlap, filling more and more of the volume. Ultimately the density and temperature span more than six orders of magnitude in such a simulation and are anticorrelated: high-density regions are cold, and low-density regions are hot. As the third column in Fig. 2 shows, this anticorrelation results in near pressure equilibrium between these two phases of the gas. Nevertheless the dense gas is about one order of magnitude lower in pressure than the low-density gas indicating that a thermal instability is active. Other regions which are out of pressure equilibrium by 1–2 orders of magnitude are those which have just experienced thermal energy input from supernovae. Self-gravitating gas would also appear out of pressure equilibrium, something we see in later stages of the simulation.

The dynamical state of the stars and of the gas in different temperature regimes in the simulation is summarized by a plot of the average velocity dispersions (Fig. 3). Guided by some of the features in the cooling curve (see Fig. 1), we divide the temperature into the following four categories: (I) $T < 2000$ K, (II) $2000 < T < 10^5$ K, (III) $10^5 < T < 4 \times 10^6$ K, (IV) 4×10^6 K $< T$. We compute the average velocity dispersion of the gas in each of these four regimes, and in addition, we calculate the mass-weighted velocity dispersion of the gas, as well as the mass-weighted velocity dispersion of the stars. As the stars are assigned the velocity of their progenitor gas at formation, their velocity dispersion closely follows the velocity dispersion of the cold gas. Furthermore, we find that with the exception of the hottest phase (IV), the velocity dispersion of the other phases approximately settles to the following values: (I) 15 km s^{-1}, (II) 30 km s^{-1} and (III) 75 km s^{-1}. What is very striking in the plot of the velocity dispersions is the high velocities ($\sim$500 km s^{-1}) attained by the hot, low-density component of the gas. The densest structures which provide the raw material for star formation, collide and break apart, but are also subject to stripping via hydrodynamical and thermal instabilities when this hot, low-density material flows rapidly past them. The picture of a 'violent interstellar medium' (McCray & Snow 1979) emerges.
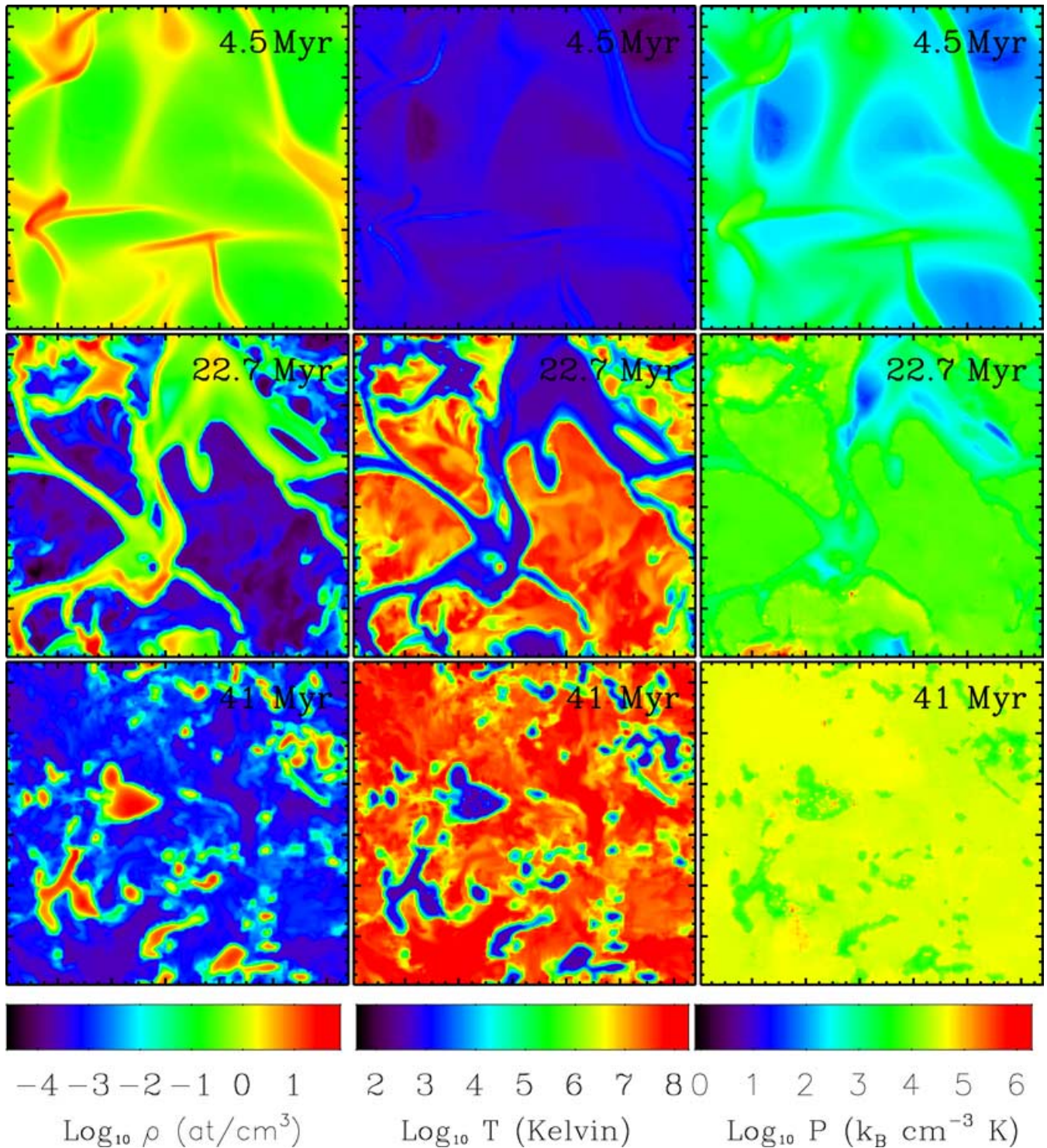
Figure 2. Time evolution of the logarithm of the gas density (first column), temperature (second column) and pressure (third column) in a 12.8 pc × 1.28 kpc × 1.28 kpc slice for run B4.

Regarding the evolution of the thermal state of the gas, this is well portrayed in phase diagrams of the gas (bottom row of Fig. 4) which show the distribution of the mass fraction of the gas as a function of its temperature and density. Given our initial conditions of uniform density and temperature, if we were to plot a phase diagram of the gas at time $t = 0$ Myr, all the gas would occupy a single point. Because the initial temperature (10^5 K) of the gas coincides with the peak of the cooling curve, by 9 Myr (first panel of bottom row

of Fig. 4) the majority of the gas quickly radiatively cools to an approximately isothermal state at a temperature corresponding to the minimum of the cooling curve, i.e. 310 K. As we instantaneously imprint a spectrum of velocity perturbations at the beginning of the simulation, the gas acquires a range of density values and therefore has a spread in densities by this time. Thereafter, with the injection of hot gas into the medium, a tail of low-density, hot gas appears. However, as gas with temperatures $10^5 < T < 4 \times 10^6$ K (phase III)
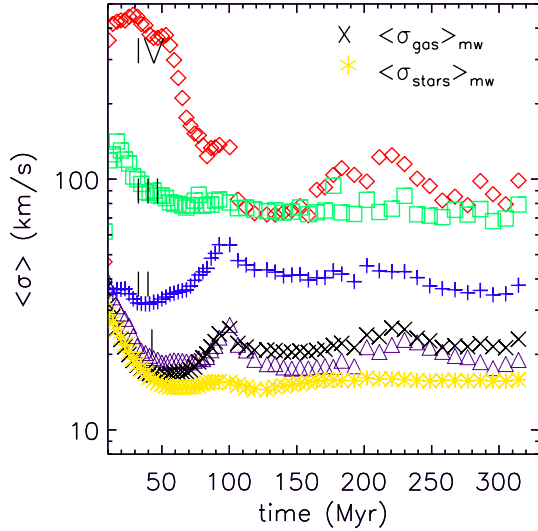
Figure 3. Time evolution of the logarithm of the velocity dispersion in run B4 for the gas in different temperature regimes: (I) $T < 2000$ K (triangles), (II) $2000 < T < 10^5$ K (plus signs), (III) $10^5 < T < 4 \times 10^6$ K (squares), (IV) 4×10^6 K $< T$ (diamonds). The crosses mark the average mass-weighted velocity dispersion of the gas and the asterisks that of the stars.

is thermally unstable, it gradually vanishes from the medium, dividing the gas into two parts in the phase diagram. The majority of the coldest ($T \sim 300$ K) gas differs by approximately a one order of magnitude pressure jump from gas with $T \geqslant 5 \times 10^5$ K. Finally the pressure of both the hot and cold gas changes with time. It rises as more and more hot gas fills the simulation volume, a situation that would probably be different if hot gas were allowed to escape the box.

Although complex, pictures of the gas density and temperature distribution in a two-dimensional slice through the simulation volume do not capture the intricacy of the three-dimensional structure. In an attempt to display this structure, in Fig. 5 we plot isodensity surfaces of the gas for $\rho = 10^{-3}$, 1, 10 and 50 atom cm^{-3} at 50 Myr. It is clear from these figures that the hot, low-density component fills most of the volume, while the densest regions fill the smallest fraction of the space, and are scattered throughout the box. A three-dimensional rendering of the stellar density at the same time instant (Fig. 6), reveals traces of the imprint of the high-density gas distribution and encouragingly bears some qualitative resemblance to the distribution of Hα emission in disc galaxies (e.g. NGC 4631; Wang et al. 2001).

4 QUANTIFYING THE STRUCTURE AND ENERGETICS OF THE MULTIPHASE MEDIUM

In an effort to assess what determines star formation rates, we systematically examine how different physical processes change the structure and the energetics of the interstellar medium. The sequence of runs listed in Table 1 is designed to isolate the effects of successively more complicated physical processes. A plot comparing the star formation rates for this sequence of runs (Fig. 7) invites us to study what keeps star formation at a minimum and alternatively what is necessary to drive it to high values. Resolution effects immediately manifest themselves in Fig. 7. The 64^3 and 128^3 runs start from the same initial conditions. Preceding star formation, feedback is non-existent, but self-gravity plays a larger role in the 64^3 run where a grid cell of equivalent density to that in the 128^3 grid is eight times more massive. Therefore in the 64^3 run with only self-gravity (run C2), the SFR rises more rapidly at earlier times than for the comparable run performed on the 128^3 grid (run B2). Once feedback occurs, a mechanism supplementary to turbulence exists for creating high density contrasts which are stronger in the
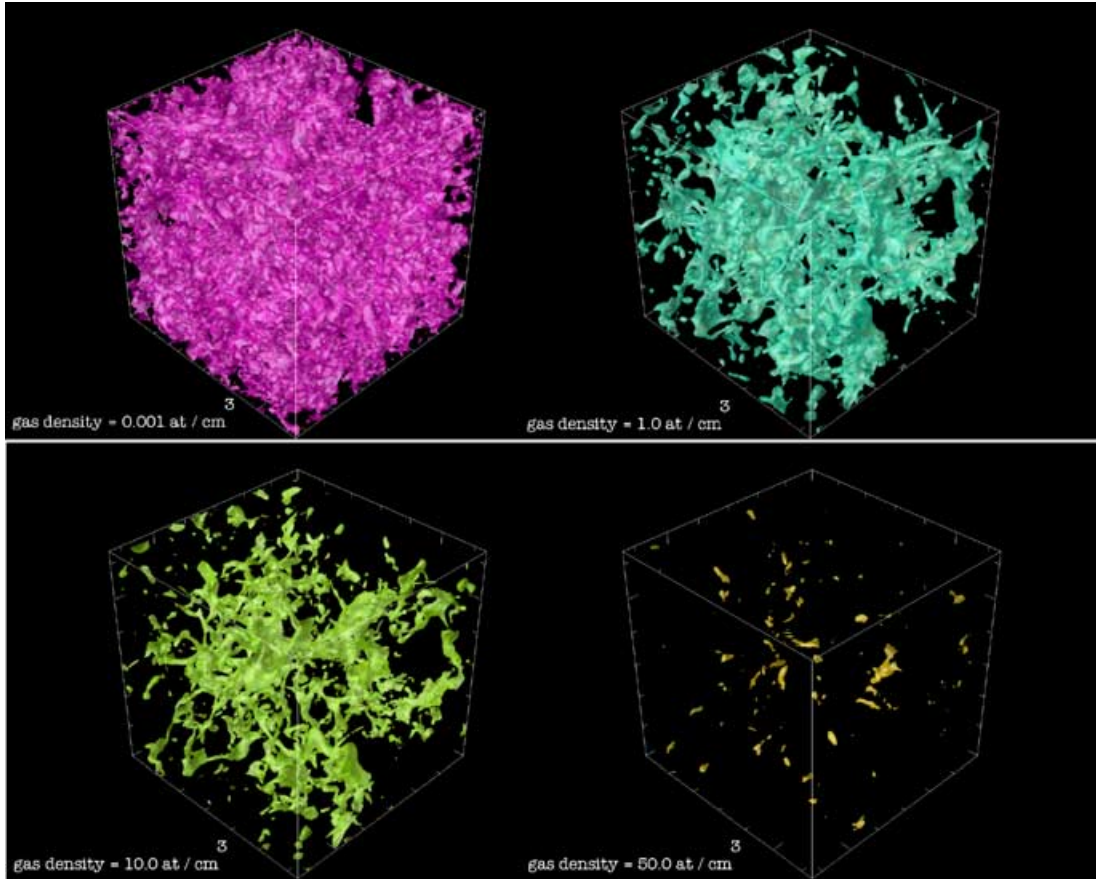
Figure 4. Time evolution of the density PDF (top row) and phase diagrams (bottom row) for run B4 (128^3 run with star formation, feedback and self-gravity). In the phase diagrams, the dotted vertical (horizontal) line marks the critical density, $\rho_{\rm crit}$ (temperature, $T_{\rm crit}$), for star formation. Dotted diagonal lines mark lines of constant pressure, and are labelled for the $t = 0$ Myr frame: $P = 10^6$, 10^5, 10^4 and 10^3 $k_{\rm B}$ cm^{-3} K. Dashed diagonal lines (labelled for the $t = 0$ Myr frame) mark the Jeans length: $\lambda_{\rm J} = 10$ pc, 34 pc, 113 pc, 380 pc and 1.28 kpc.

Figure 5. Isodensity surfaces of the gas for run B4 and $\rho = 10^{-3}$, 1, 10 and 50 atom cm^{-3}.

higher resolution runs. This causes higher peaks of SFR in the 128^3 runs with feedback (runs B3 and B4) as compared to the equivalent 64^3 runs (C3 and C4). On the other hand, feedback also creates an extra source of pressure to fight self-gravity which explains why the C2 run leads to higher SFRs at earlier times than the C3 and C4 runs. What remains unclear without performing a simulation at still higher resolution is whether the indistinguishability between the 128^3 runs with feedback regardless of whether or not there is self-gravity (runs B3 and B4) is a manifestation of convergence or

coincidence. However, we believe convergence is the more probable explanation as increasing the resolution tends to increase the dominance of feedback processes over self-gravity. More specifically, in the case of the 64^3 runs a rise in the SFR is driven more rapidly when self-gravity is included. In contrast, star formation increases at similar rates regardless of whether self-gravity is included in the 128^3 runs. Therefore we do not see any reason why this trend should be inverted by further increasing the resolution.

Before proceeding, we calculate roughly the supernovae rate corresponding to the measured star formation rates in our simulations. In our 1.28^3 kpc^3 box, typical star formation rates are SFR $\sim$0.1 –0.8 M$_\odot$ yr^{-1}. Scaling these values to a Milky Way type galaxy, where M_{MW} is the mass of gas in the Milky Way, and M_{box} is the mass of gas in our simulation cube,

$$\text{SFR} \, (M_{MW}/M_{box}) \approx 100\text{–}800 \, M_\odot \, \text{yr}^{-1}. \tag{2}$$

For a Salpeter IMF there is approximately 1 SN/200 M$_\odot$, implying that the typical supernovae rates in our simulation volume are $\sim$0.5 –4 SN yr^{-1}. Furthermore, with this scaling to higher mass the projected gas surface density increases by about four orders of magnitude bringing both the SFRs and surface densities to values representative of the starburst regime in the Kennicutt relation (Kennicutt 1998).

A visual examination of a 2D snapshot of the gas density, temperature and pressure taken at the same time ($t = 45$ Myr) for runs including different physics is useful for comparing some of the consequences of the different processes. Fig. 8 clearly shows how self-gravity, which is a radially directed force towards regions of locally high density, causes high-density regions to take on a
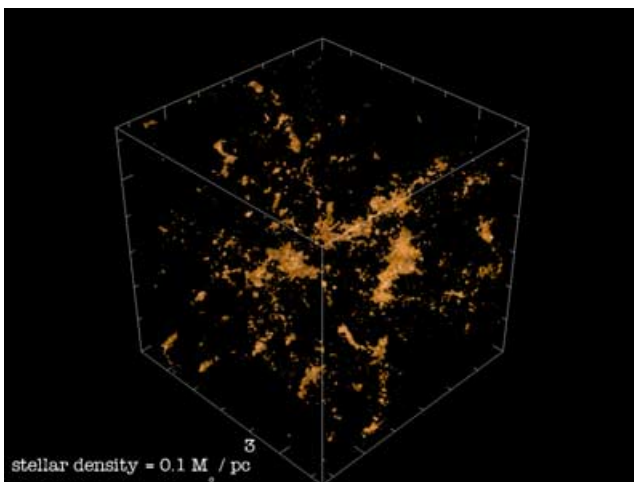

Figure 6. Isodensity surface of the stellar density for run B4 and $\rho_\star = 0.1$ M$_\odot$/pc^3.
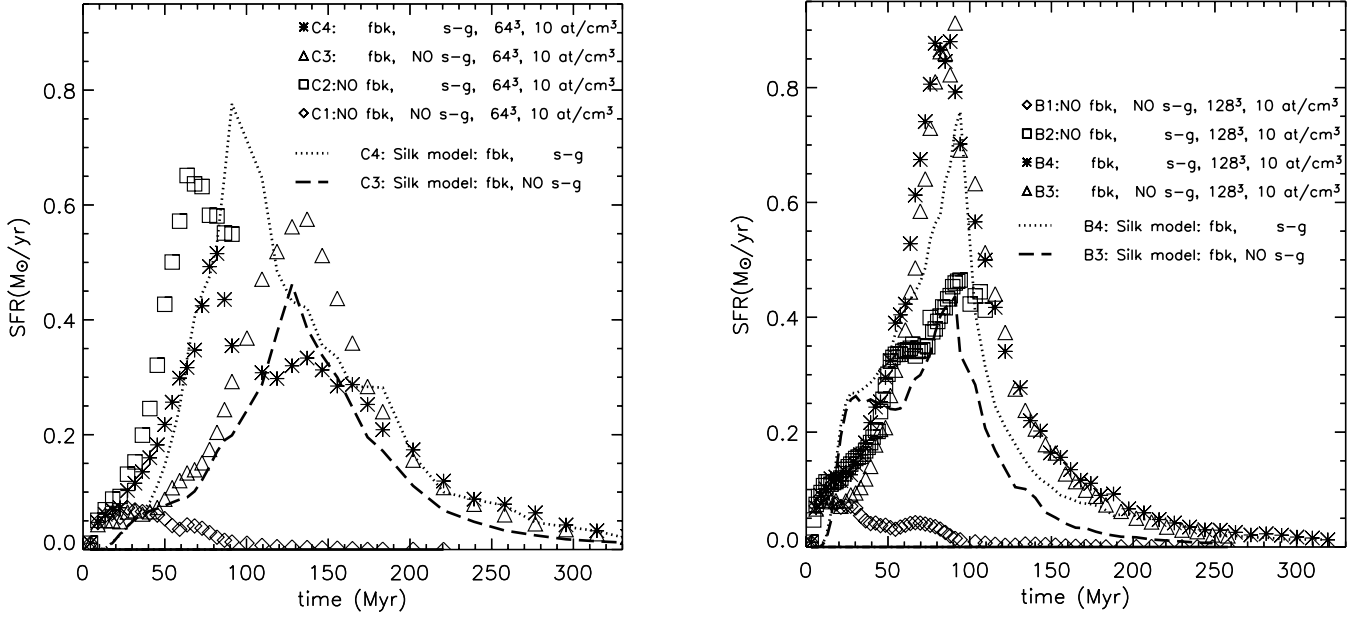
Figure 7. Time evolution of the star formation rate for a series of runs (see Table 1) differing in their physics. The left panel displays the results from runs C1 (diamonds), C2 (squares), C3 (triangles) and C4 (asterisks). The right panel displays the results from runs B1 (diamonds), B2 (squares), B3 (triangles) and B4 (asterisks). Symbols are the measured SFRs and the dotted and dashed lines are analytic models from Silk (2001).
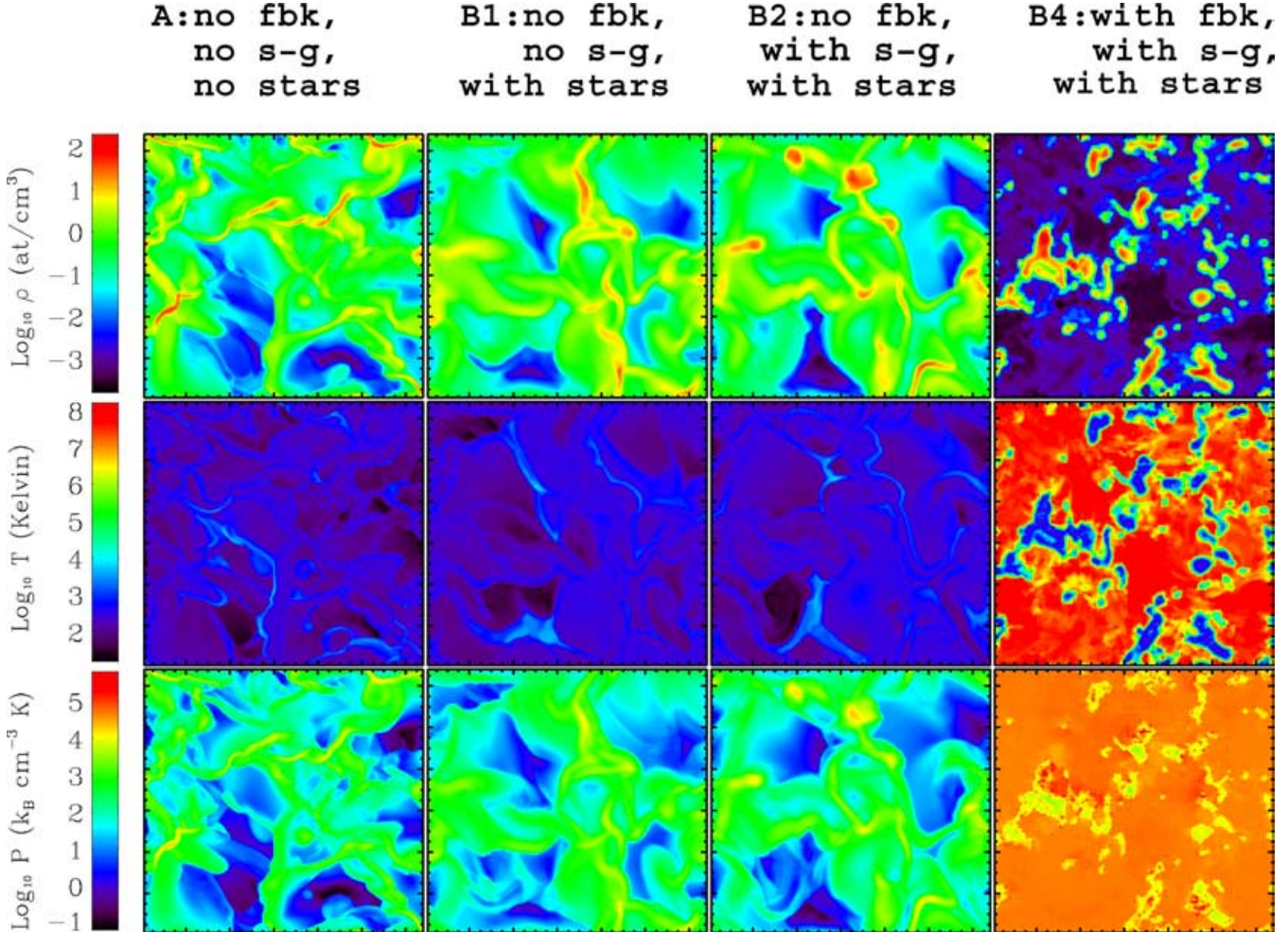

Figure 8. The gas density, temperature and pressure at time $t = 45$ Myr in a 12.8 pc $\times$ 1.28 kpc $\times$ 1.28 kpc slice for runs A, B1, B2 and B4 (see Table 1 for the specifications of each of these runs).

more spherical appearance. Furthermore, all the runs without feedback have gas with pressure spanning over approximately six orders of magnitude, and a small range in temperatures compared to the run with feedback. The low-density gas regions in the runs without feedback are cold ($T \sim 300$ K) and are created by adiabatic cooling during extreme expansion in certain regions of the 'turbulent' medium. Another feature that appears in this sequence of simulations is that the dense structures in the run with feedback are sharper due to destruction of intermediate density material by thermal and hydrodynamical instabilities.

4.1 Probability density function of mass density

A density probability distribution function (PDF) is a simple one-dimensional statistical measure of the structure of a medium. In practice, for simulations performed on a grid, PDFs are instantaneous histograms tallying the number of grid cells of a certain density in the simulation. Under the premise that stars form in high-density regions, the statistical properties of the density field, itself non-linearly coupled to the velocity field, might give clues to the process of star formation. Efforts to uncover how the gas density organizes itself in media structured by different dynamical processes are ongoing. Vázquez-Semadeni (1994) presented a statistical argument to show that turbulent (random), supersonic, compressible flows naturally generate hierarchical structure without necessitating an appeal to things like fragmentation in a gravitationally unstable system (Hoyle 1953). In the limit of very high Mach numbers these flows have a pressureless behaviour and if, in addition, self-gravity is negligible then the hydrodynamical equations are scale-invariant. Consequently, whatever the density in a given region, that region has the same probability of producing a relative fluctuation with respect to its normalizing density, as any other region in the flow. Assuming that in a random flow successive density steps are independent, the central limit theorem dictates that the density distribution should be log-normal. And indeed, the two-dimensional, essentially isothermal ($\gamma = 1.0001$) simulations of Vázquez-Semadeni (1994) of a weakly compressible ($M \sim 1$), turbulent flow without self-gravity developed log-normal density PDFs both on the large scale of the simulation and in subregions within the simulation.

Subsequently, numerical experiments of three-dimensional, isothermal, randomly forced, supersonic turbulence by Padoan, Nordlund & Jones (1997) also found that the gas density follows a log-normal distribution,

$$\text{PDF} = \frac{1}{\sigma\sqrt{2\pi}}\, e^{-(\ln\rho - \langle\ln\rho\rangle)^2/2\sigma^2}. \tag{3}$$

Furthermore they observed empirically that the dispersion, σ, of the log-normal scales with the root-mean-squared Mach number, M_{rms}, as follows:

$$\sigma^2 = \ln\left[1 + \left(\frac{M_{\text{rms}}}{2}\right)^2\right] \tag{4}$$

or, for the case of linear dispersion,

$$\sigma_{\text{linear}} = \frac{M_{\text{rms}}}{2}. \tag{5}$$

These dispersion relations reflect the fact that in a medium with higher M_{rms}, the gas achieves greater density contrasts. Passot & Vázquez-Semadeni (1998) found the same linear scaling relation for the isothermal case. A formal proof for the log-normal PDF in the case of isothermal, supersonic turbulence was provided by Nordlund & Padoan (1999) based on the formalism given in Pope & Ching (1993).

Scalo et al. (1998) and Passot & Vázquez-Semadeni (1998) extended this work on isothermal flows by considering the polytropic case. Having conducted two-dimensional simulations including various combinations of physical processes (e.g. self-gravity, magnetohydrodynamics, Burgers turbulence), Scalo et al. (1998) found PDFs that were more consistent with power laws than with log-normal distributions. Seeking to understand this result and its discrepancy with previous work on isothermal flows which consistently found log-normal distributions, Scalo et al. (1998) performed one-dimensional simulations of forced, supersonic, polytropic turbulence and uncovered a log-normal PDF for the cases where either the gas was isothermal ($\gamma = 1$) or where the Mach number was small ($M \ll 1$). Otherwise, when $\gamma < 1$, power laws developed for densities larger than the mean. Alternatively, Nordlund & Padoan (1999) interpreted the results of Scalo et al. for the PDFs occurring in the $\gamma \neq 1$ case as skewed log-normals and Passot & Vázquez-Semadeni (1998) provided a mathematical framework for understanding why these distributions arose.

Our work extends these investigations on the PDF in the direction of the cases where the ISM is constrained neither to be isothermal nor polytropic. As a result our local temperature and pressure are not simple functions of the density but arise from the evolution of the thermal energy. Because we consider processes (e.g. radiative cooling, self-gravity, star formation) whose effectiveness depends on the density, the hydrodynamic equations are no longer scale-invariant. Therefore the condition of randomness between subsequent density fluctuations is violated and one cannot expect a log-normal density PDF (e.g. Vázquez-Semadeni 1994). In our series of experiments of increasing complexity (see Table 1), the simplest simulation we performed was of non-isothermal supersonic turbulence (run A). Despite the inclusion of density-dependent cooling processes, we found that the structure of the gas quickly evolved to a density PDF consistent with a log-normal. This is not a surprising result since without a heat source the majority of the gas quickly cools to a nearly isothermal state (see bottom row of Fig. 9) with an average temperature corresponding to the minimum of the cooling curve (horizontal dashed line in bottom row of Fig. 9). Furthermore, the scaling for the dispersion of the PDF given by Padoan et al. (1997) continued to hold. In fact, rather than fit log-normal functions to our density PDFs, we measured the average of the logarithm of the gas density, $\langle\log_{10}\rho\rangle$, and the M_{rms} of the gas at different time instances and then overplotted the prediction of Padoan et al. (1997) for the log-normal distribution. For the runs where we formed stars (without self-gravity or feedback) in addition to having radiative cooling (runs B1 and C1), the gas density PDF continued to have the same behaviour: the M_{rms} of the system progressively declined with time, while the density PDF remained consistent with a log-normal distribution (Fig. 10).

The runs which showed the first departure from log-normal density PDFs were the runs which included self-gravity (runs B2 and C2) but still no feedback (Fig. 11). Repeating the exercise of measuring the average of the logarithm of the gas density, $\langle\log_{10}\rho\rangle$, and the M_{rms} of the gas at different times, we found two differences: (a) the M_{rms} initially declined but then stabilized at a value higher than that seen in the runs without self-gravity, and (b) the log-normal PDF predicted by Padoan et al. (1997) consistently underpredicted the distribution at high gas density. A power law fitted the high-density tail well. In one-dimensional simulations of Burgers flows, i.e. infinitely compressible flows, power laws were also found to be good fits to the density PDFs (Gotoh & Kraichnan 1993). We therefore interpret the power-law behaviour for the run with self-gravity, as reflecting the added possibility of the gas, once it has a high density,
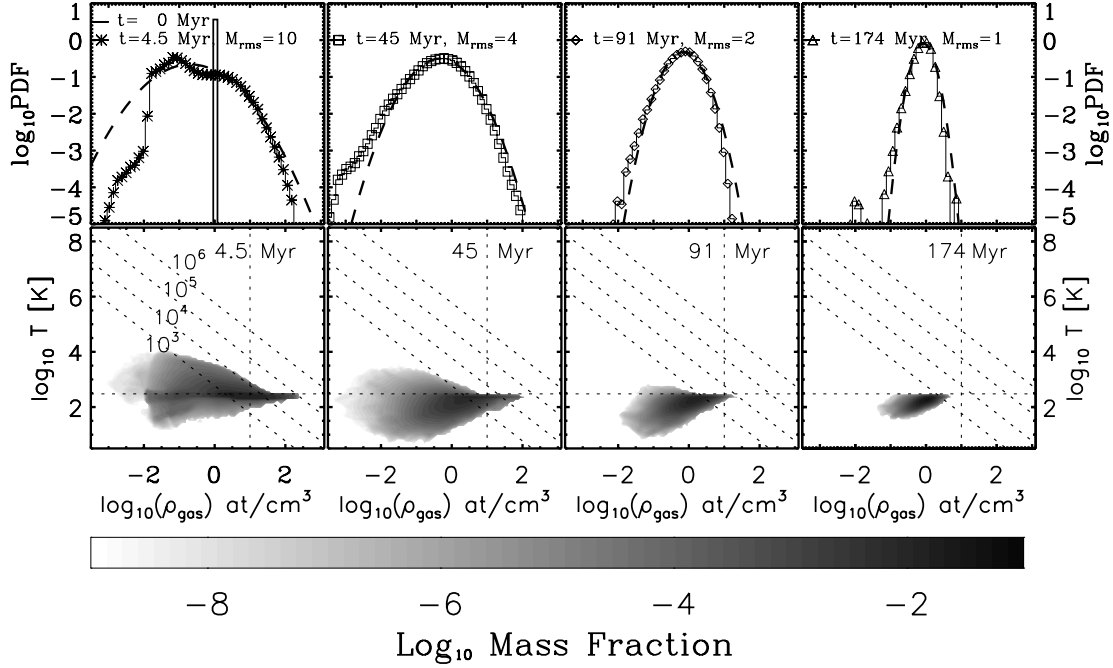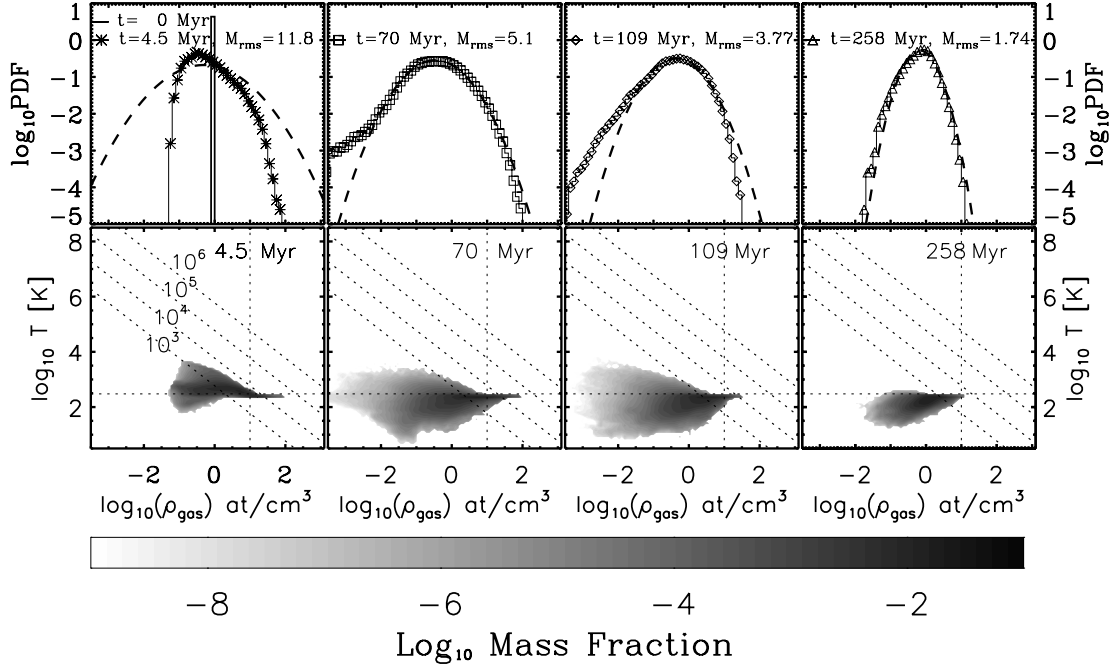
Figure 9. Time evolution of the density PDF (top row) and phase diagrams (bottom row) for run A (128^3 run with no star formation, no feedback and no self-gravity). The thick dashed line overplotted on the measured PDFs (symbols) is the log-normal PDF predicted by Padoan et al. (1997). In the phase diagrams, the dotted vertical (horizontal) line marks the critical density, ρ_{crit} (temperature, T_{crit}), for star formation. Dotted diagonal lines mark lines of constant pressure, and are labelled for the $t = 0$ Myr frame: $P = 10^6$, 10^5, 10^4 and $10^3 k_B$ cm^{-3} K.

Figure 10. Time evolution of the density PDF (top row) and phase diagrams (bottom row) for run B1 (128^3 run with star formation, no self-gravity, and no feedback). The thick dashed line overplotted on the measured PDFs (symbols) is the log-normal PDF predicted by Padoan et al. (1997). In the phase diagrams, the dotted vertical (horizontal) line marks the critical density, ρ_{crit} (temperature, T_{crit}), for star formation. Dotted diagonal lines mark lines of constant pressure, and are labelled for the $t = 0$ Myr frame: $P = 10^6$, 10^5, 10^4 and $10^3 k_B$ cm^{-3} K.

to compress to even higher density, reminiscent of the behaviour in Burgers flows. Klessen (2000) also explored the form of the density PDF for the cases of decaying and driven self-gravitating turbulence. Although he found a departure from log-normal at high densities, the departure could not be characterized by a power law.

When we add feedback to the list of simulated processes, either with self-gravity (runs B4 and C4) or without (runs B3 and C3), the density PDF becomes markedly bimodal (Fig. 12), illustrating that most of the simulation volume is occupied by low-density gas. A bimodal density distribution is also a sign of a thermal
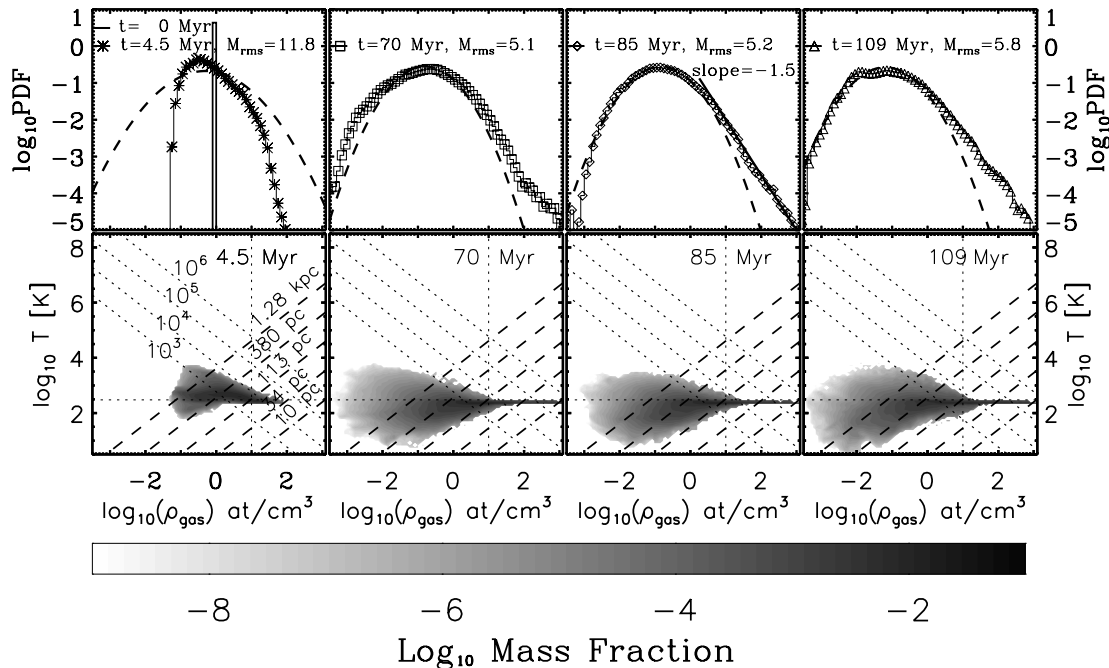
Figure 11. Time evolution of the density PDF (top row) and phase diagrams (bottom row) for run B2 (128^3 run with star formation and self-gravity but no feedback). The thick dashed line overplotted on the measured PDFs (symbols) is the log-normal PDF predicted by Padoan et al. (1997). The solid line with a slope of -1.5 plotted at $t = 85$ Myr is a fit to the high-density end of the PDF. In the phase diagrams, the dotted vertical (horizontal) line marks the critical density, ρ_{crit} (temperature, T_{crit}), for star formation. Dotted diagonal lines mark lines of constant pressure, and are labelled for the $t = 0$ Myr frame: $P = 10^6$, 10^5, 10^4 and $10^3 \, k_B \, cm^{-3}$ K.
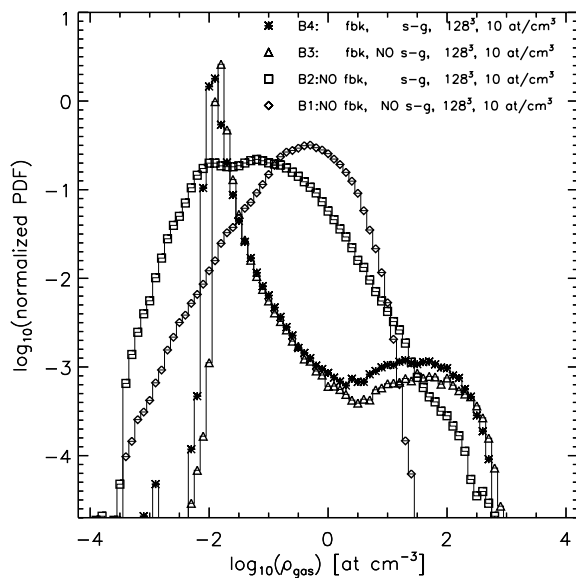

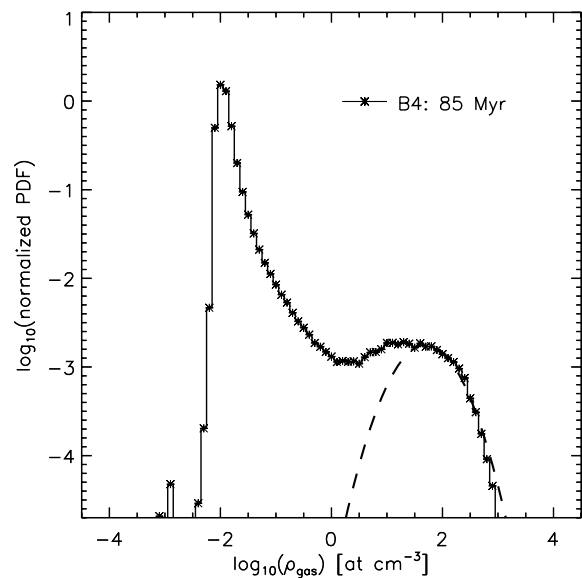**Figure 12.** Comparison of the PDFs at 110 Myr for runs with different physics.

Figure 13. Log-normal fit to high-density end of the PDF for run B4 at $t = 85$ Myr. The scaling we use for the fit is a log-normal with average density of $10^{1.7}$ atom cm^{-3} and with a dispersion of $\sim 10^{1.22}$ atom cm^{-3}.

instability (Vázquez-Semadeni, Gazol & Scalo 2000) the consequences of which we will discuss in a future paper (Slyz, Devriendt, Bryan & Silk, in preparation). For the runs with self-gravity, the high-density power-law tail disappears. Perhaps it can be argued that the high-density part of the density PDF may be fitted with a log-normal distribution (Fig. 13). The exercise of overplotting the log-normal given by Padoan et al. (1997) is not possible because the M_{rms} measured for the entire simulation box does not correspond to the M_{rms} of the high-density gas for which the log-normal function

may be a good description. Hence we can only *fit* log-normals to the high-density gas, similar to what others, e.g. Wada & Norman (2001), Kravtsov (2003) do in their global simulations of the ISM.

The interest of describing the density structure of the ISM with a single function, such as the log-normal, lies in finding a link between the gas density averaged over kiloparsec sized regions and the high-density regions which might form stars. This is precisely the link required for an explanation of the Schmidt law. Rewriting

the Schmidt law in a form where the star formation rate is equal to some constants multiplied by the fraction of gas in high-density regions and by the gas density averaged over large scales (his equation 7), Elmegreen (2002) emphasized that star formation rates depend on the geometry of the density field, i.e. the PDF. If the shape of the density PDF is universal, then the fraction of gas in high-density regions is known. Consequently, if the high-density regions are also self-gravitating, then the fraction of gas available for star formation is also known. Admittedly, the density PDF contains no spatial information, hence there is no reason for which the high-density regions should find themselves to be spatially contiguous, so that they comprise regions of mass greater than the Jeans mass. In fact, Fig. 11 clearly shows that at least some of the dense gas regions are not contiguous because if they were they would simply not persist as all the gas would be converted to stars on a dynamical time-scale since these regions are well above $\rho_{\rm crit}$ and cold. We therefore have to identify these regions with divergent gas flows.

A two-dimensional study of the ISM in a galactic disc by Wada & Norman (2001) has claimed that the log-normal distribution is a robust description of the ISM density distribution over many orders of magnitude in density, regardless of the simulated physics. More specifically, in their simulations the presence of stellar feedback does not change the shape of the PDF but increases the dispersion of the log-normal. In three-dimensional simulations of a high-redshift galaxy performed in a cosmological context, Kravtsov (2003) finds a density distribution similar to Wada & Norman (2001). Its shape at every redshift epoch has a flat region at $\rho_{\rm gas} \leqslant 1$ –10 $M_\odot$ pc^{-3} and a power-law distribution at high densities. He claims that the log-normal distribution is a fair description of the high-density tail of the PDF and agrees with Wada & Norman (2001) on the insensitivity of the distribution to feedback, except at the low-density end, where the simulation with feedback produces more low-density gas. As Fig. 12 shows, our less realistic study of star formation occurring in a periodic box without the global gravitational galactic potential or the shear instabilities present in a self-gravitating rotating disc, appears to be more sensitive to the input physics. Only the runs which include stellar feedback are nearly equivalent, regardless of whether there is self-gravity. When log-normals are overplotted for the runs without feedback, the position of the maximum of the log-normal is shifted to lower densities by more than one order of magnitude from the position of the maximum of the log-normal fit to the high-density part of the PDF for the runs with feedback. Indeed the densities in certain cells for the run with only self-gravity reach the same high values as the runs with feedback, but a much smaller fraction of the simulation volume has these high densities. Another blatant difference between the PDFs we find in our runs with feedback and the PDFs found by Wada & Norman (2001) and Kravtsov (2003) is that their runs do not show as high a peak at low densities. The smaller quantity of low-density gas in their simulations is likely due to the much lower supernovae rates in the simulations of Wada & Norman (2001) (0.01 SN yr^{-1} as compared to 0.5–4 SN yr^{-1} in our simulations) and in the case of Kravtsov (2003), to the more realistic boundary conditions, which allow tenuous, hot gas to escape the disc.

4.2 Energy spectra

Energy spectra of the ISM carry complementary information to that given by a study of its density structure. With the density PDFs, we confirmed that in many cases there exists a clear relationship between the density contrast achieved and the $M_{\rm rms}$ of a system (i.e. $\sigma_{\rm linear} \sim M_{\rm rms}$). But the $M_{\rm rms}$ of a system is only a global measure-

ment of its kinetic energy content. With measurements of the kinetic energy spectra, we expect to learn how the energy is distributed on different spatial scales and how the different physical processes we considered influence the time evolution of this distribution.

The Kolmogorov theory of incompressible, subsonic turbulence predicts that energy fed on large scales progressively cascades to smaller scales until it is dissipated by molecular viscosity on the smallest scales in vortex rings. The transfer of energy is a local process and the spectra of the velocity field is a power law with $E_k \sim k^{-5/3}$ (Kolmogorov 1941). With supersonic, compressible turbulence, strong shocks come into play. They allow energy to be transferred over widely separated scales and it is possible that rather than being dissipated in vortex rings, the energy is ultimately dissipated in sheets, filaments and cores (Boldyrev 2002). Given the analogy between highly supersonic and pressureless flows, one might expect the compressible, supersonic flows to have the same behaviour as Burgers turbulence with power spectra in the inertial regime of the form $E_k \sim k^{-2}$ (Burgers 1974; Gotoh & Kraichnan 1993). However, this appears to be true only in one and two dimensions. In three dimensions, compressible, supersonic flows differ from Burgers flows because they generate vorticity (Boldyrev 2002). In three-dimensional simulations of compressible, supersonic, magnetized forced turbulence with Mach number initially $\sim$10, Boldyrev, Nordlund & Padoan (2002) find energy power spectra in the inertial range to be $E_k \sim k^{-1.74}$, i.e. close to the Kolmogorov value.

As we lack the grid resolution to ascertain if the energy spectra in our simulations are tending towards power laws, we cannot make any credible statements about the values of the power-law slopes. Furthermore in incompressible turbulence, the energy spectrum is a power law in the inertial regime (at k wavenumbers below the energy injection scale but above the energy dissipation scale). In our simulations the feedback energy is injected on scales equivalent to the grid resolution, i.e. the smallest scales, but it can propagate to larger scales depending on the ISM dynamics. Therefore for the runs with feedback the inertial regime has a more complicated meaning. Instead in Fig. 14 we focus on the time development of the energy spectra, and the presence of characteristic features. The standard approach involves dividing the kinetic energy into two components: a compressible one for which $\nabla \times v_{\rm comp} = 0$, and a solenoidal one with $\nabla \cdot v_{\rm sol} = 0$. In words, the compressible component measures the strength of the shocks in the system, while the solenoidal component measures the degree of rotation. Typically, the compressible component is expected to decay faster than the solenoidal component as the shock energy is transformed into vortical eddy motions.

Because we remove gas from the system to form stars, the kinetic energy whose spectra we measure is rather a specific kinetic energy, i.e. we divide the instantaneous total kinetic energy by the total gas mass present at that moment. In all our runs, the kinetic energy which is initially imprinted only on large scales quickly (within $\sim$30 Myr) redistributes itself to smaller scales as well. Following this redistribution, for the run with neither self-gravity nor feedback (run B1), the compressible and solenoidal components of the energy spectra progressively decay, all the while maintaining approximately the same form. The ratio $E_{\rm c}/E_{\rm s}$ is always less than 1, i.e. the compressible component decays faster than the solenoidal one, but increases towards the dissipative regime. In high-resolution simulations (512^3, 1024^3) of decaying compressible turbulence with Mach number initially on the order of 1 (an order of magnitude lower than the initial Mach number in our simulations), Porter, Woodward & Pouquet (1998) find a similar result with $E_{\rm c}/E_{\rm s} \sim 0.1$. In contrast to these runs in which the kinetic energy decays, the runs with self-gravity (run B2) and/or feedback (runs B3, B4), show energy
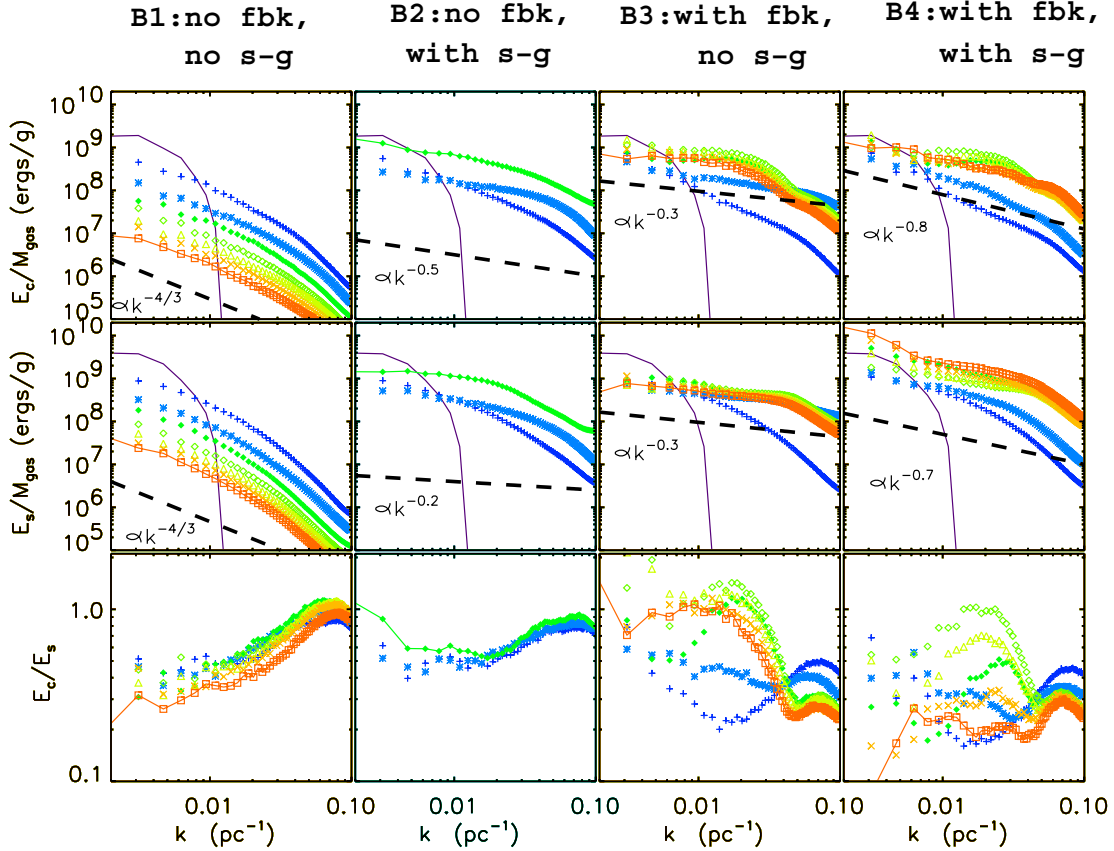
Figure 14. Time evolution of the compressible (E_c) and solenoidal (E_s) components of the energy spectra for runs B1, B2, B3 and B4. Symbols denote energy spectra at time intervals separated by 30 Myr. The solid line represents time $t = 0$ Myr. Plus signs: 30 Myr; asterisks: 60 Myr; filled diamonds: 90 Myr; open diamonds: 120 Myr; open triangles: 150 Myr; crosses: 180 Myr; open squares: 210 Myr. We also draw a solid line through the symbols when they represent the final time-step that we are displaying. Thick dashed lines indicate power laws with slopes similar to that of the last curve shown.

spectra which climb to higher amplitudes with time and have shallower slopes than the decaying run (B1). Furthermore in plots of the ratios of the compressible to solenoidal components, between 90 and 150 Myr the runs with feedback show a peak at ∼65 pc consistent with what one would predict for the characteristic length-scale for a simulation with supernovae expanding into a medium with ambient pressure of $P = 10^6 \, \mathrm{cm}^{-3} \, \mathrm{K} \, k_B$. More explicitly, ignoring adiabatic and radiative losses, a supernova with 10^{51} erg of energy will be halted by an ambient medium at this pressure when it has expanded to a radius $r \sim (E/P)^{1/3} \sim 65$ pc. This signature in E_c/E_s for the run with feedback points to a way to understand SFRs, which we explore below.

5 NUMERICAL VERSUS ANALYTICAL STAR FORMATION RATES

An alternative to searching for a generic density PDF as an explanation for star formation rates, is to consider arguments concerning the competition between the expansion of supernovae remnants and the pressure which halts them. In this vein, Silk (1997, 2001) developed porosity models of a regulated ISM. Introduced by Cox & Smith (1974), the porosity, Q, is proportional to the product of the supernovae rate per unit volume and the maximum extent of the 4-volume of the supernovae remnants. In other words, the porosity measures the fraction of hot gas, f_h, in the ISM through the relation $Q = -\ln(1 - f_h)$. Silk reasoned that since the supernovae production rate

is proportional to the star formation rate (SFR), and the maximum extent of a supernova remnant is limited by the ambient pressure, the following expression arises:

$$Q = \mathrm{SFR} \, G^{-1/2} \, \rho_{\mathrm{gas}}^{-3/2} \, (\sigma_{\mathrm{gas}}/\sigma_{\mathrm{f}})^{-2.72} \tag{6}$$

where ρ_{gas} is the gas density, σ_{gas} is the gas velocity dispersion, and σ_{f} is a fiducial velocity dispersion that is proportional to $E_{\mathrm{SN}}^{1.27} \, m_{\mathrm{SN}}^{-1} \, \zeta_{\mathrm{g}}^{-0.2}$. Here E_{SN} is the energy of a single supernova, ζ_{g} is the metallicity relative to solar of the ambient gas, and m_{SN} is the mean mass in newly formed stars required to produce a supernova. For $E_{\mathrm{SN}} = 10^{51}$ erg, $\zeta_{\mathrm{g}} = 1$, and $m_{\mathrm{SN}} = 250 \, \mathrm{M}_\odot$, i.e. the case where we assume only the occurrence of Type II supernovae with a Miller–Scalo IMF, the fiducial velocity dispersion is ∼22 km s⁻¹.

Our simulations with feedback provided a laboratory to test this analytic description of the SFR. For the purpose of computing the porosity of the medium, we measured the fraction of hot gas in our volume, defining hot to be gas with temperature $T \geqslant 4 \times 10^6$ K. For ρ_{gas} in equation (6) we took the average gas density in our simulation volume, and for σ_{gas} we took the average mass-weighted velocity dispersion of the gas. We kept the value for σ_{f} at 22 km s⁻¹. Given these values as functions of time, we plotted as dotted and dashed lines the expectation from equation (6) for the SFRs in Fig. 7. Computing the actual star formation rates in the box by defining the mass of newly formed stars to be the mass of stars formed in the past 3 Myr, we overplotted the results as symbols in the same figure.

Astonishingly, the analytic values match the measured rates to better than a factor 2.

Given the simplifications in the derivation of the analytic model, there was no a priori reason for the fit to be a good description of the star formation rate in an inhomogenous, non-stationary model of the ISM. For example, Silk takes the expression for the 4-volume of the SNR remnant in its cooling phase from Cioffi, McKee & Berschinger (1988). They derive it under the assumptions that the supernova expands in a spherical manner, the ISM is homogenous and uniform (i.e. no density gradients), there is no dust cooling or thermal conduction, and the ambient ISM pressure is negligible until the last stage of supernova evolution when the remnant merges with the ambient ISM. In contrast, we find that at least in the initial stages of our simulations, the supernovae remnants are highly non-spherical, the ISM is inhomogeneous with ubiquitous density gradients and the ambient ISM gas pressure is highly non-negligible ($P = 10^5$–10^6 cm^{-3} K k_B). However, as more of the gas turns into stars, and the hot phase fills the majority of the simulation volume, the ISM does start to resemble something more in line with the assumptions of Cioffi et al.

When we examine in Fig. 15 the time evolution of each of the physical quantities entering into the analytic model for the SFR, we find the following. The runs (B1 and C1) which produced the lowest star formation rates have zero porosity and high fractions of cold gas ($f_{cold} \sim 0.8$–0.9), but a continuously declining velocity dispersion. The runs reaching a peak (runs B2, B3, B4, C2, C3) or multiple

peaks of high star formation (run C4) all displayed depleted cold gas fractions after their final star formation peak, a rise to a maximum in its velocity dispersion at the peak, and either zero porosity for the case of the runs with self-gravity but no feedback (runs B2 and C2) or a porosity that levels off to a constant value around the time of the SFR peak [$Q \sim 4$–5 for the 64^3 case (runs C3 and C4), and $Q \sim 4$ for the 128^3 case (runs B3 and B4) after the SFR peak]. We interpret the behaviour in these parameters as reflecting the importance of a high velocity dispersion for generating high SFRs. Indeed in the analytic model for the SFR (equation 6), the gas velocity dispersion, σ_{gas}, plays the most important role, as it is raised to the highest power in the expression. However, even with velocity dispersions sustained at high values ($\sigma_{gas} \sim 20$ km s^{-1}), SFRs will drop if the reserves of cold gas decline.

6 DISCUSSION

Given the simplicity of our simulations, we examine their relevance for representing true star formation processes in real galaxies. The first issue we address is whether the star formation rates we obtain are consistent with the Kennicutt relation. In Section 4 we scaled the mass in our simulation volume to that of the Milky Way, finding that our star formation rates and surface densities were consistent with star formation occurring in the starburst regime. If we do not scale our SFRs and gas densities to a Milky Way type galaxy but instead take them at face value we find that our initial 1 atom cm^{-3} gas density in a $(1.28$ kpc$)^3$ volume yields in projection about a 30 M$_\odot$ pc^{-2} column density which lies at the boundary between Kennicutt's normal discs and centres of normal discs (Kennicutt 1998). Transforming our average star formation rate of 0.2–0.3 M$_\odot$ yr^{-1} into a star formation rate per unit volume leads us to an average star formation rate density of about 0.1 M$_\odot$ yr^{-1} kpc^{-2}, on the high side but in fair agreement with Kennicutt's measurements for our computed surface density (Kennicutt 1998, fig. 6). We note that Kennicutt's law is a static relation as it concerns space-averaged quantities in local galaxies, and a moment in the history of these galaxies is bound to exist when their main progenitor will be entirely gaseous (i.e. with no stars yet formed) and the Kennicutt relation will break. As our simulations start from an exclusively gaseous medium, we do not expect our simulation to follow the Kennicutt relation from the very beginning, but to move towards it as it does. We nevertheless consider our simulations to be in a starburst mode because the duration of the star formation episode is much shorter than that of what one expects in either a disc or spheroidal galaxy. But this is not unusual since we are only modelling a chunk of a galaxy and are therefore neglecting effects on larger length- and therefore time-scales.

The second issue we address is whether periodic boundary conditions drive the high star formation rates seen in our simulations. When hot gas starts to fill the bulk of the simulation volume, because the boundary conditions trap the hot gas, conditions in the simulation may be viewed as a pressure cooker and the increased pressure may drive higher star formation rates. In our simulation by the time the pressure cooker is operative, the SFRs are already at starburst levels as seen when one scales the SFRs and gas densities to a Milky Way type galaxy as we do in Section 4. To be more specific, for the pressure cooker to be operative we have to wait ~10 Myr for the first supernovae to go off and then we have to wait for the volume to become significantly filled by this supernovae generated hot gas for the hot gas to be able to traverse the volume unobstructed by cold, dense gas. According to Fig. 15, it takes on the order of 50 Myr for the hot gas filling fraction to be approximately 50 per cent,
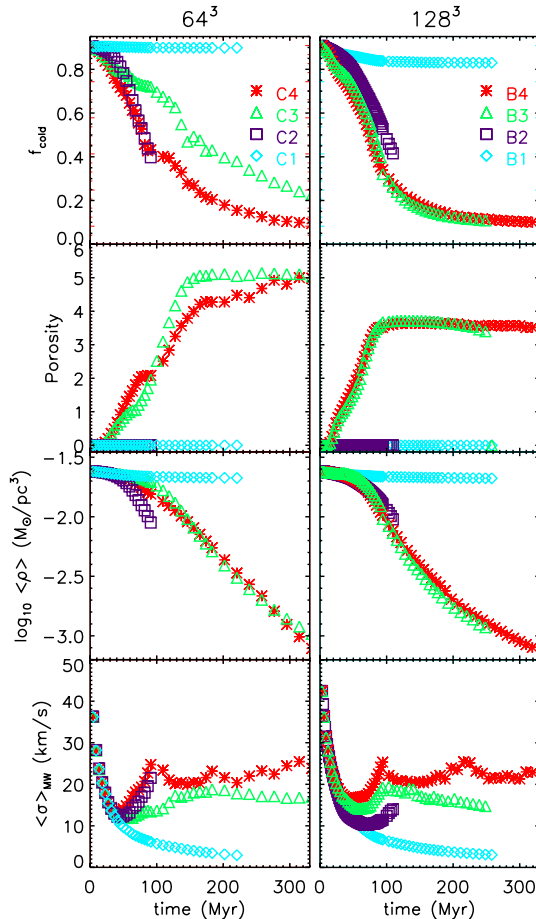

Figure 15. Plots comparing the time evolution of the cold mass fraction, porosity, average gas density, and mass-weighted velocity dispersion for runs containing different physics, on the 64^3 and 128^3 grid.

corresponding to a porosity of about 0.7. Hence boundary effects are not dominant in shaping the star formation rate until after that time. We also point out that the limitations of the boundary conditions should not obfuscate the point that the manner in which we implement supernovae is a more important factor leading to the build up of large quantities of hot gas in the medium. When we perform simulations in all points identical to those presented in this paper but with supernovae going off instantaneously, as opposed to exploding with a more realistic 10 Myr time delay used in the work presented in this paper, we get extremely low star formation rates (a few hundred times smaller than those we get in our simulation here), because the hot gas never fills a significant fraction of the simulation cube. In other words, the periodic boundary conditions cannot dominate the physics of star formation driven by hot gas pressure until the hot gas has already been generated, and we find that this depends strongly on the way the supernovae are implemented. As mentioned in Section 1, we leave the discussion of this to a future paper.

The limitations of our closed, periodic box, and the absence of a stratified external gravitational potential certainly keep our simulations far from being representative of realistic galactic systems. For example, a credible simulation of a disc galaxy would have to be performed in a realistic cosmological context to capture such effects as tidal encounters and stripping from neighbours. Excluding these external stellar heating processes as well as spiral waves, results in the neglect of processes that would increase the velocity dispersion of the stars in real galaxies. Therefore our simulations certainly have a higher fraction of cold ISM and cold stars after a gas consumption time which may prolong and strengthen star formation in our simulations.

We also emphasize that with our crude assumption of a closed box not only can no material escape the box, affecting star formation rates once hot gas permeates the simulation volume, but no material can enter the simulation volume either. It could well be that accretion of cold material is more relevant for star formation in real discs than either the external star heating processes missing from the simulations discussed above or the fact that hot gas cannot leave the simulation volume. One can argue that perhaps the simulations presented in this paper are more representative of what happens in the central kiloparsec of a spheroidal starburst galaxy. In that case the potential well might indeed trap a fraction of the hot gas and the pressure cooker environment which comes into play after high star formation rates occur in the simulation, if not as drastic as in our simulations, might well be fairly realistic.

7 SUMMARY AND CONCLUSIONS

To unravel which global parameters control star formation, we have examined star formation occurring in media whose dynamics are structured by various combinations of physical processes (e.g. 'turbulence', radiative cooling, self-gravity, feedback from supernovae and stellar winds). We sought to understand our models of the ISM from structural and dynamical perspectives, finding that in some cases there was a well-defined link between the two. In particular, measurements of the density PDFs confirmed that for the simulations without feedback, log-normals were an adequate description of the structure of the medium, and that the density contrasts achieved in the media were directly correlated to their M_{rms}. Log-normals consistently underpredicted the high-density end of the runs with self-gravity which appeared to be well-fitted by a power law. For the runs with feedback, the dense gas reached higher densities than those reached by the runs without feedback, implying that in these simulations, feedback was positive in the sense that it encouraged

higher star formation rates. However, the PDF for the runs with feedback had a distinctly bimodal shape with the majority of the volume filled by low-density gas. In summary, we did not find a universal PDF. Most markedly, runs with feedback had a different PDF from the runs without feedback, although arguably the high-density end might be fitted by a log-normal.

Measurements of the energy spectra in our simulations were consistent with the information provided by the density PDFs. Self-gravity alone was sufficient to sustain the kinetic energy of the medium, and hence maintain the high density contrast we observed in the PDFs. Feedback also succeeded in keeping high quantities of kinetic energy in the media and inspection of ratios of compressible to solenoidal energy revealed that supernovae were pumping energy into the system at a characteristic scale consistent with the ambient pressure in the hot, low-density component of the medium.

For the runs with feedback, comparing the Silk (2001) star formation model to the measured values of the SFRs in our simulations revealed a good match that led us to inspect the parameters involved in Silk's prescription. They showed clearly that the SFR depends strongly on the underlying velocity field which we saw could be energized by self-gravity and/or feedback to produce high density contrasts. Without a means to create these high densities, star formation rates decline even in the presence of a large reservoir of cold gas.

In light of the issues neglected in our simulations, we stress that the simplifying assumptions made in this paper facilitated our choice to start from as strong a local physical basis as possible before trying to tackle star formation in a more global context. As such we neglect numerous physical processes which may invalidate partially or completely our current results, but this remains to be addressed in future work. Nevertheless we hope that the present work sheds some light on the local physics that should be included in future realistic simulations of star formation.

REFERENCES

Avillez M. A., 2000, MNRAS, 315, 479
Begelman M. C., Fabin A. C., 1990, MNRAS, 244, 26
Bhatnagar P. L., Gross E. P., Krook M., 1954, Phys. Rev., 94, 511
Boldyrev S., 2002, ApJ, 569, 841
Boldyrev S., Nordlund Å., Padoan P., 2002, ApJ, 573, 678
Brinks E., Bajaja E., 1986, A&A, 169, 14
Bryan G. L., Norman M. L., 1997, in Clarke D. A., Fall M., eds, ASP Conf. Ser. Vol. 123, Computational Astrophysics. Astron. Soc. Pac., San Francisco, p. 363
Bryan G. L., Norman M. L., 1999, in Chrisochoides N., ed., Workshop on Structured Adaptive Mesh Refinement Grid Methods. IMA Volumes in Mathematics 117. Springer, New York, p. 165
Burgers J. M., 1974, The Nonlinear Diffusion Equation. Reidel, Dordrecht
Cen R., Ostriker J. P., 1992, ApJ, 399, L113
Cioffi D. F., McKee C. F., Berschinger E., 1988, ApJ, 334, 252
Cox D. P., Smith B. W., 1974, ApJ, 189, L105
Dettmar R.-J., 1992, Fund. Cosmic Phys., 15, 143
Deul E. R., den Hartog R. H., 1990, A&A, 229, 362
Elmegreen B. G., Kim S., Stavely-Smith L., 2001, ApJ, 548, 749
Elmegreen B. G., 2002, ApJ, 577, 206

Ferguson A. M. N., Wyse R. F. G., Gallagher J. S., 1996, AJ, 112, 2567
Gotoh T., Kraichnan R. H., 1993, Phys. Fluids A, 5, 445
Heiles C., 1979, ApJ, 229, 533
Heiles C., 1984, ApJS, 55, 585
Hoyle F., 1953, ApJ, 118, 513
Irwin J. A., 1994, ApJ, 429, 618
Kennicutt R. C., 1998, ApJ, 498, 541
King D. Irwin J. A., 1997, NewA, 2, 251
Klessen R. S., 2000, ApJ, 535, 869
Kolmogorov A. N., 1941, Dokl. Akad. Nauk SSSR, 30, 301
Korpi M. J., Brandenburg A., Shukurov A., Tuominen I., 1999a, A&A, 350, 230
Korpi M. J., Brandenburg A., Shukurov A., Tuominen I., Nordlund Å., 1999b, ApJ, 514L, 99
Kravtsov A. V., 2003, ApJ, 590, L1
Lee S.-W., Irwin J. A., 1997, ApJ, 490, 247
McCray R., Snow T. P., 1979, ARA&A, 17, 213
MacLow M.-M., Klessen R. S., Burkert A., Smith M. D., 1998, Phys. Rev. Lett., 80, 2754
Marri S., White S. D. M., 2003, MNRAS, 345, 561
Nordlund Å., Padoan P., 1999, in Franco J., Carramiñana A., eds, Interstellar Turbulence. Cambridge Univ. Press, Cambridge, p. 218
Ostriker J. P., Cowie L. L., 1981, ApJ, 243, L127
Padoan P., Nordlund Å., Jones B., 1997, MNRAS, 288, 145
Passot T., Vázquez-Semadeni E., 1998, Phys. Rev. E, 58, 4501
Pope S. B., Ching E. S. C., 1993, Phys. Fluids A, 5, 1529
Porter D. H., Woodward P. R., Pouquet A., 1998, Phys. Fluids, 10, 237

Prendergast K. H., Xu K., 1993, J. Comput. Phys., 109, 53
Rand R. J., van der Hulst J. M., 1993, AJ, 105, 2098
Rand R. J., Kulkarni S. R., Hester J. J., 1990, ApJ, 352, L1
Rosen A., Bregman J. N., 1995, ApJ, 440, 634
Rosen A., Bregman J. N., Norman M. L., 1993, ApJ, 413, 137
Sarazin C. L., White R. E., 1987, ApJ, 320, 32
Scalo J. M., Vázquez-Semadeni E., Chappell D., Passot T., 1998, ApJ, 504, 835
Schmidt M., 1959, ApJ, 129, 243
Silk J., 1997, ApJ, 481, 703
Silk J., 2001, MNRAS, 324, 313
Slavin J. D., Shull J. M., Begelman M. C., 1993, ApJ, 407, 83
Slyz A., Prendergast K. H., 1999, A&AS, 139, 199
Spitzer L., 1956, ApJ, 124, 20
Stanimirovic S., Staveley-Smith L., Dickey J. M., Sault R. J., Snowden S. L., 1999, MNRAS, 302, 417
Tenorio-Tagle G., 1981, A&A, 94, 338
Vázquez-Semadeni E., 1994, ApJ, 423, 681
Vázquez-Semadeni E., Gazol A., Scalo J., 2000, ApJ, 540, 271
Wada K., Norman C. A., 2001, ApJ, 547, 172
Wang Q. D., Immler S., Walterbos R., Lauroesch J. T., Breitschwerdt D., 2001, ApJ, 555, L99
Xu K., 1998, Gas-Kinetic Schemes for Unsteady Compressible Flow Simulations. VKI report 1998–03

This paper has been typeset from a TEX/LATEX file prepared by the author.